RESEARCH ARTICLE

Tailoring Breathing Behavior of Solid Electrolyte Interphases Unraveled by Cryogenic Transmission Electron Microscopy

Xuyun Guo, Xiaoqiong Du, Valeria Nicolosi, Biao Zhang,* and Ye Zhu*

The cycling stability of batteries is closely related to the dynamic evolution of solid electrolyte interphases (SEIs) in response to the discharging/charging processes. Here, the state-of-the-art cryogenic transmission electron microscopy (cryo-TEM) and spectroscopy are utilized to probe the SEI breathing behavior induced by discharging/charging on the conversion-type anode made of Fe_2O_3 quasi-cubes. The incorporation of the identical-location strategy allows the tracking of the evolution of the same SEIs at different charge states. SEI breathing is shown to involve swelling (contracting) upon lithiation (de-lithiation) driven by the reversible compositional change. Bare Fe_2O_3 anodes develop an unstable SEI layer due to the intermixing with the lithiation product Li_2O, which exhibits a large thickness variation upon breathing as well as excessive growth. A transition from organic to inorganic-type SEI is also identified upon cycling, which gives rise to significantly increased SEI resistance. To tailor the SEI behavior, N-doped carbon coating is applied on Fe_2O_3 (Fe_2O_3@CN), which can effectively separate the lithiation product from SEI. A thinner and chemically more stable SEI layer develops on Fe_2O_3@CN, resulting in remarkably enhanced cycling stability compared to bare Fe_2O_3. This work demonstrates the importance of understanding and optimizing the dynamic behavior of SEIs to achieve better battery performance.

1. Introduction

Solid electrolyte interphases (SEIs) play an irreplaceable role in rechargeable batteries.[1] Due to the higher Fermi levels of anodes relative to the lowest unoccupied molecular orbital (LUMO) of electrolytes, electrons migrate from anodes to electrolytes to trigger electrolyte decomposition and result in SEIs on the anode surface.[2] SEIs mainly form in the first few cycles typically consisting of both inorganic and organic species,[3] which feature a large irreversible capacity and low initial Coulombic efficiency (ICE).[4] The desirable SEI layers need to be ionically conducting but electronically insulating, which is essential for conducting reversible discharging/charging reactions without further electrolyte decomposition.[5] Tremendous research efforts have been dedicated to understanding the SEI formation and properties, aiming to optimize battery performance.[6] Both electrolyte and anode surface can directly affect the characteristics of SEIs, including thickness,[7] morphology,[8] and composition,[9] which further impacts the cyclic performance. For instance, the chemical composition of SEIs especially the distribution of inorganic components critically affects their ionic conductivity and mechanical stability, playing a critical role in battery stability.[10] An optimized SEI layer can passivate the anode surface and maintain its integrity upon cycling with self-limiting thickness, which enables long-term stability without electrolyte degradation; while, the repeated cracking and healing process of an unstable SEI layer can lead to continuous consumption of electrolyte and working ions, causing irreversible capacity loss upon cycling.[11]

With the significant progress on understanding their structure and properties, SEIs have still been acknowledged as the least understood component in batteries, with many aspects remaining elusive. In particular, all the discharging/charging processes must go through SEIs, which may alter their characteristics dynamically and lead to distinct properties at different charge states. The drastic change in the operation condition, the electrochemical environment, and the anode volume upon discharging/charging cycling may also cause the dynamic response of SEIs. In spite of early studies revealing the development of SEIs after increasing number of cycles,[12] the dynamic behavior of SEIs at different charge states was not systematically investigated until Bryngelsson et al. who utilized X-ray photoelectron spectroscopy (XPS) to unveil the swelling (contracting) of the SEI layer upon lithiation (de-lithiation) on a graphite anode, with the disparate SEI composition also identified between the two processes.[13] Such SEI "breathing" behavior[14] has been further observed on various materials including the conversion-type Fe_2O_3 anode and the novel Si

X. Guo, X. Du, B. Zhang, Y. Zhu
Department of Applied Physics
Research Institute for Smart Energy
The Hong Kong Polytechnic University
Hung Hom, Kowloon, Hong Kong, P. R. China
E-mail: biao.ap.zhang@polyu.edu.hk; yezhu@polyu.edu.hk

X. Guo, X. Du, V. Nicolosi
School of Chemistry
Centre for Research on Adaptive Nanostructures and Nanodevices
(CRANN) and Advanced Materials Bio-Engineering Research Centre
(AMBER)
Trinity College Dublin
Dublin D02PN40, Ireland

The ORCID identification number(s) for the author(s) of this article can be found under https://doi.org/10.1002/aenm.202300240.

anodes (Table S1, Supporting Information).[15] All these pioneering works mainly used spectroscopy-based approaches to probe SEIs. Even though there is an agreement on the dynamic nature of SEIs, the opposite SEI breathing behavior in response to lithiation/de-lithiation was reported,[15b–d] leaving controversy in this underexplored phenomenon. Moreover, the origin of SEI breathing behavior may be associated with the reversible formation of some inorganic/organic compounds,[16] but exactly what components of SEIs may react reversibly during discharging/charging cycling is still largely unknown. Given that SEI breathing could potentially influence both stability and capacity of batteries,[17] it demands further investigation, especially the direct microscopic observation with chemical sensitivity, to better elucidate such dynamic behavior.

Cryogenic transmission electron microscopy (cryo-TEM) has been recently demonstrated as a powerful tool to image radiation-sensitive electrode materials and SEIs at the atomic level.[18] Applying cryo-TEM in the ex situ manner, the dynamic behavior of SEIs has been revealed on Si[16a,19] and Li metal anodes.[20] On the other hand, most of the cryo-TEM works only compared SEIs from different samples after discharging/charging, rather than tracking the evolution of the same SEIs. It leads to the inevitable question whether the identified SEI difference truly reflects its dynamic evolution or is actually due to sample-to-sample variations. To address this question, we here incorporate the identical-location strategy to the state-of-the-art cryo-TEM, which allows us to directly compare the same SEIs at different charge states. Using this setup, we probe SEIs on the conversion-type Fe_2O_3 anode, whose SEI breathing behavior has never been observed microscopically. The Fe_2O_3 anode materials are synthesized with the unique morphology of quasi-cubes and well-defined facets, enabling easy identification of SEI layers developed on top. We explicitly unveil the SEI breathing behavior and the associated structural and chemical evolution, which lasts up to ten cycles. Long-term cycling has also been carried out to derive the influence of SEI breathing on the electrochemical stability. We further apply N-doped carbon coating to remarkably enhance electrochemical cycling. This model system provides a platform to disclose the effect of carbon coating on the SEI breathing behavior, explaining the underlying SEI origin for this widely adopted strategy in boosting the battery's stability.

2. Results and Discussion

2.1. SEI Breathing on Bare Fe_2O_3

Fe_2O_3 is synthesized by the hydrothermal method as detailed in the Experimental Section. X-ray diffraction (XRD, **Figure 1**a) identifies the obtained phase to be hematite α-Fe_2O_3 (PDF#00-001-1053) without any noticeable trace of the second phase. Electron energy loss spectroscopy (EELS, Figure 1b) mapping confirms the constituent elements of Fe and O. High-angle annular dark-field scanning TEM imaging (HAADF-STEM, Figure 1c,e) and selected area electron diffraction (SAED, Figure 1d) further reveal that α-Fe_2O_3 is in the form of single-crystal quasi-cubes ≈200 nm in size, with $\{1\bar{1}2\}$- and $\{0\,1\,2\}$-terminated surface facets. Using the backscattered electrons (BSE)

to acquire surface-sensitive images in STEM, the BSE-STEM image in Figure 1f better illustrates the well-defined flat facets, which offer an ideal base to study the behavior of SEIs developed on top. Electrochemical performance of Fe_2O_3 quasi-cubes is tested in Li-ion half cells. Even though a high reversible capacity of ≈936.5 mAh g^{-1} with 75.9% ICE is obtained in the first cycle (Figure 1g), an obvious capacity fading can be seen within the first 100 cycles (black curve in Figure 1i).

To investigate the structure origin for the cycling instability of Fe_2O_3 quasi-cubes, we perform cryo-S/TEM with the identical-location strategy to track the evolution of both Fe_2O_3 and the developed SEI upon discharging/charging cycling. To minimize the potential effects of beam exposure on the behavior of susceptible SEI, we only carry out two S/TEM observations on each tracked sample, that is, one pristine and one after cycling in the coin cell. As shown in **Figure 2**a,b, after the first discharging (lithiation), the Fe_2O_3 quasi-cube becomes inflated and coarsened, covered by a very thick and low-density SEI layer ≈74.3 nm as indicated by the lower intensity shell. The SEI appears to be porous as shown in Figure 2c, presumably owing to the gas (H_2, CO_2, or C_2H_4) generation associated with the debased decomposition of carbonate-based electrolyte solvents on Fe_2O_3 surface during SEI formation.[21] High-resolution TEM (HRTEM) identifies that the SEI consists of Li_2O (COD #1010064 in Crystallography Open Database) nanocrystals embedded in an amorphous matrix (Figure 2d), as verified by both SAED (Figure 2f) and Li K-edge EELS fine structures (Figure 2g).[22]

EELS mapping also detects the presence of C, O, and Li elements throughout the whole SEI layer (Figure 2e), resulting in the low-density shell in Figure 2b. As no C is detected in pristine Fe_2O_3 (Figure S1, Supporting Information), it must be the product of electrolyte decomposition during SEI formation and constitutes the amorphous matrix observed in Figure 2d. EELS fine structures further reveal the presence of C=C and C=O bonding, as indicated by their characteristic edges shown in Figure 2g. The weak C=C bonds may come from ethylene and fluoroethylene carbonate (FEC) derived products with alkene groups: The former is the product when ethylene carbonate (EC) is reduced to organic lithium ethylene di-carbonate (LEDC) or mono-carbonate (LEMC),[23] while the latter is related to FEC decomposition.[24] The C=O bonds could be related to Li_2CO_3, polymerized vinylene carbonate (poly(VC)), and lithium alkyl carbonates such as lithium methyl carbonate (LMC), LEDC, and LEMC species.[25] As the presence of Li_2CO_3 cannot be detected by SAED, HRTEM, or EELS fine structures, its content in the SEI should be relatively low and the detected C=O signal is primarily from the amorphous organic carbonates in SEI. On the other hand, EELS mapping unveils that the inner quasi-cube contains mostly Fe with little O and Li (Figure 2e), indicating the formation of metallic Fe from the lithiation reaction (Equation (1)), which has also been confirmed by the SAED pattern shown in Figure 2f. The absence of Li_2O in the Fe core is further verified by EELS fine structures (Figure S2, Supporting Information), which suggests that the lithiation reaction is conducted through the diffusion of O onto the surface to oxidize Li, leaving reduced metallic Fe in the core and a thick Li_2O layer on the surface. This may be due to the faster diffusivity of O than Fe in Fe_2O_3 lattice.[26] Given that such Li_2O is uniformly intermixed with the amorphous C-rich phase from
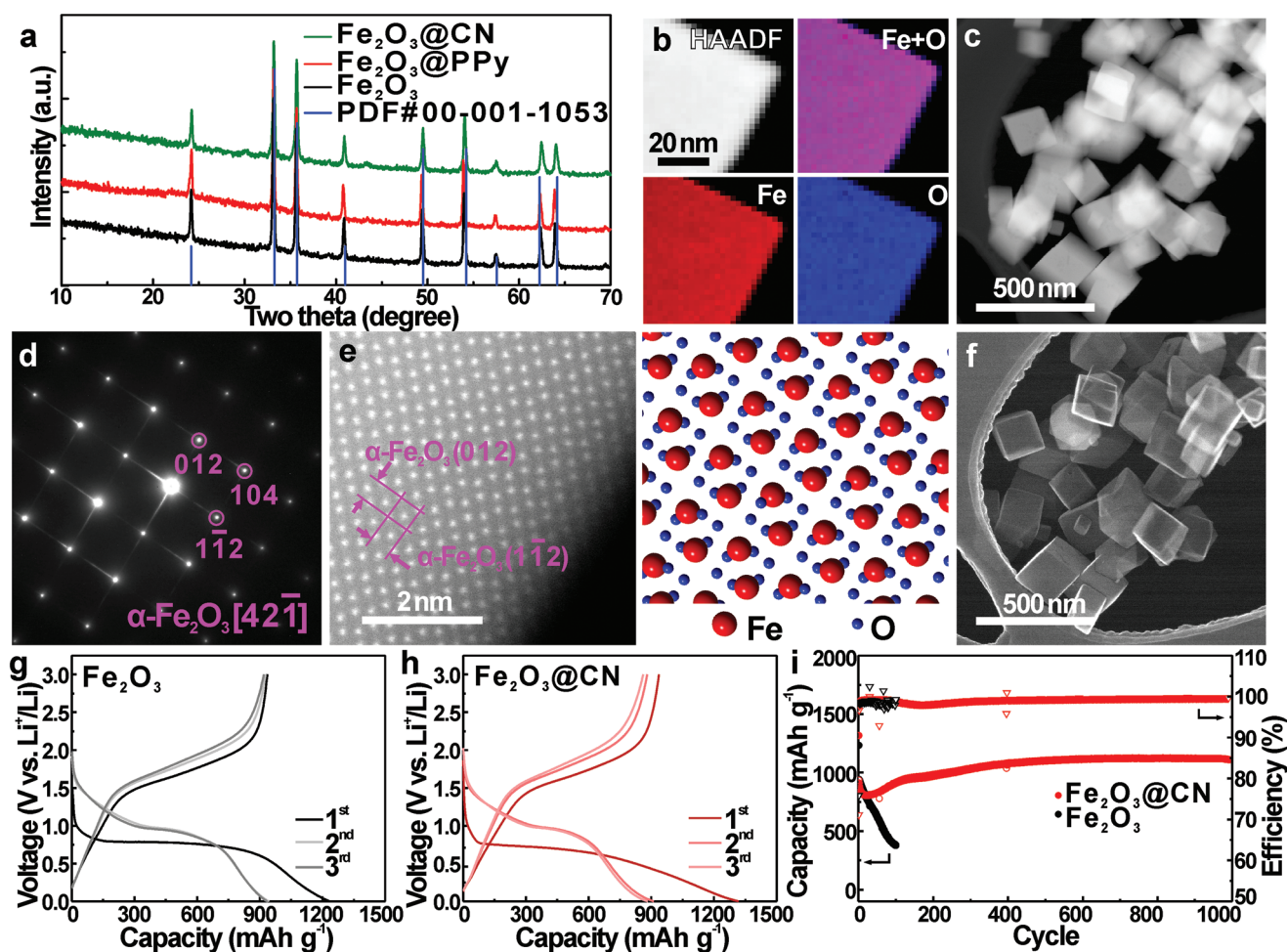
Figure 1. Characterization and electrochemical performance of Fe₂O₃ quasi-cubes. a) XRD patterns of Fe_2O_3, polypyrrole coated Fe_2O_3 (Fe_2O_3@PPy), and N-doped carbon coated Fe_2O_3 (Fe_2O_3@CN) with the standard pattern of α-Fe_2O_3 (PDF#00-001-1053) at the bottom. b) HAADF-STEM image and EELS maps. c) HAADF-STEM image. d) SAED pattern. e) Aberration-corrected HAADF STEM (AC-HAADF-STEM) image and corresponding atomic model of α-Fe_2O_3. f) BSE-STEM image (the same area as [c]) of Fe_2O_3 quasi-cubes. Selected galvanostatic discharge and charge curves of g) Fe_2O_3 and h) Fe_2O_3@CN under the current density of 1 A g⁻¹. i) Cyclic performance of Fe_2O_3 and Fe_2O_3@CN under the current density of 1 A g⁻¹.

electrolyte decomposition, we still consider it as part of the SEI in this analysis.

$$Fe_2O_3 + 6Li^+ + 6e^- \rightarrow 3Li_2O + 2Fe \quad (1)$$
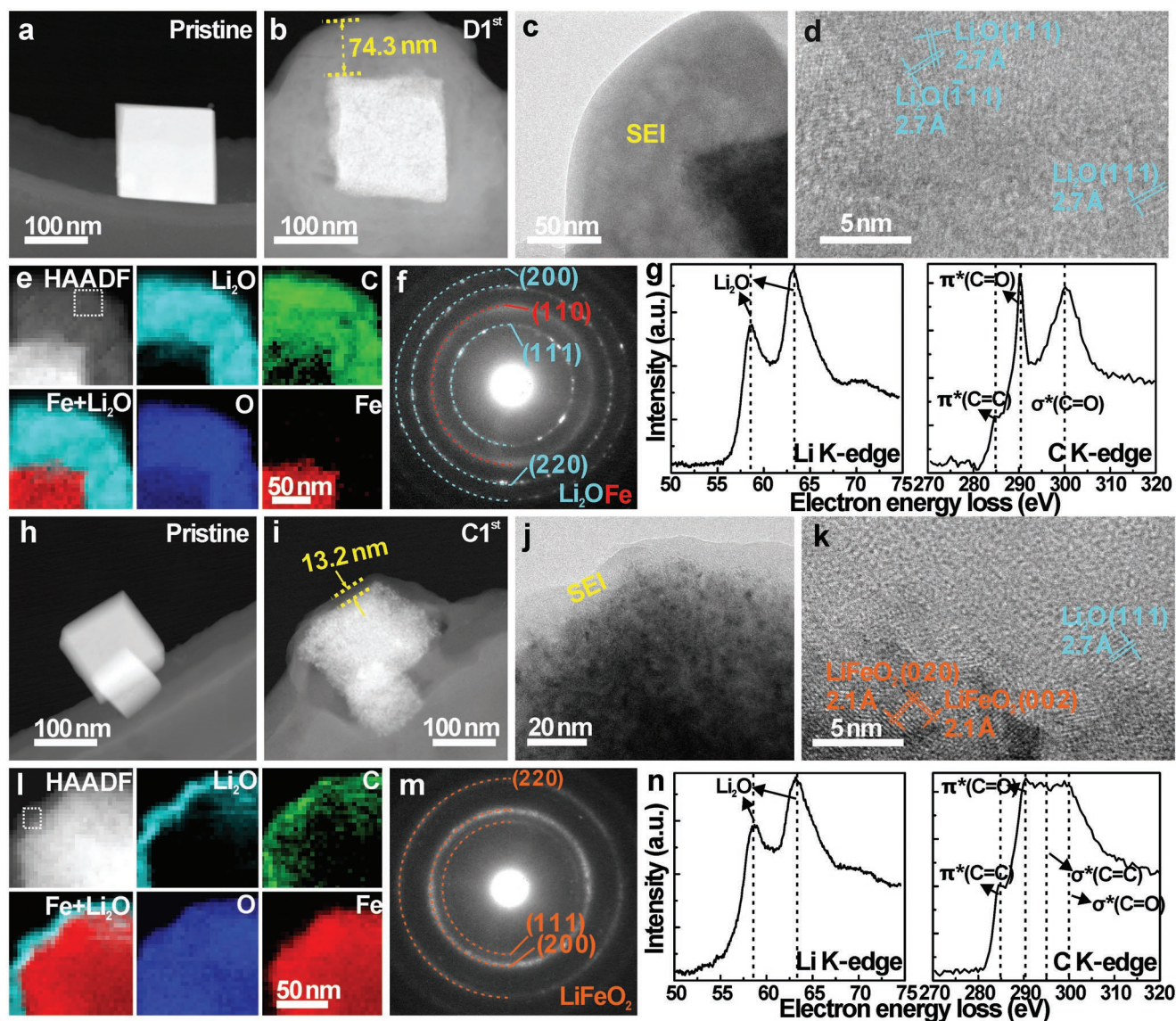
$$2Li_2O + Fe - 3e^- \rightarrow LiFeO_2 + 3Li^+ \quad (2)$$
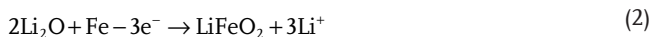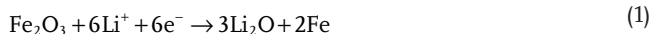
Strikingly, after the first charging (de-lithiation), the SEI thickness dramatically reduces to only ≈13.2 nm (Figure 2h–j), demonstrating SEI breathing upon discharging/charging cycling. HRTEM identifies the presence of both $LiFeO_2$ (COD #1541312 in Crystallography Open Database) and residual Li_2O nanocrystals (Figure 2k). SAED further shows that $LiFeO_2$ is the dominant Fe phase after the full charging (Figure 2m), which should form from oxidation of Fe in contact with Li_2O following Equation (2), in line with the previous study.[27] The formation of $LiFeO_2$ rather than Fe_2O_3 has been attributed to the difficulty of losing one electron for $LiFeO_2$ to be fully de-lithiated under the normal potential.[28] Both HRTEM (Figure 2k) and EELS fine structures (Figure 2n) confirm the

presence of residual Li_2O in the SEI layer, which however cannot be detected by SAED (Figure 2m), probably owing to their ultrasmall particle size with rather weak diffraction signals. Moreover, the C K-edge after de-lithiation (Figure 2n) presents remarkable difference compared with the fully discharged state (Figure 2g), with substantial enhancement of C=C signal relative to C=O. This suggests that the carbon species with C=O bonding as identified in lithiated SEI diminishes upon de-lithiation, which is responsible for the declined SEI thickness. Therefore, the observed SEI breathing can be attributed to the reversible reaction of C=O containing species as well as Li_2O upon discharging/charging cycling.

The SEI breathing continues in the subsequent discharging/charging cycles. As shown in Figure S3, Supporting Information, the SEI formed on the Fe_2O_3 quasi-cube after 10th discharge also has a large thickness of ≈67.8 nm and abundant Li_2O (Figure S3a–f, Supporting Information). After full charging, the SEI thickness reduces to ≈15.8 nm (Figure S3g–l, Supporting Information), slightly thicker than that after the first cycle (≈13.2 nm) and still with the formation of $LiFeO_2$ in

**ADVANCED
SCIENCE NEWS**

www.advancedsciencenews.com

**ADVANCED
ENERGY
MATERIALS**

www.advenergymat.de

Figure 2. Identical-location cryo-S/TEM characterization of SEI formed on bare Fe_2O_3 quasi-cubes in the first cycle. a–g) HAADF-STEM images of an Fe_2O_3 quasi-cube before (a) and after (b) the first full discharge (D1st), and the corresponding TEM (c) and HRTEM images (d). HAADF-STEM image and EELS maps (e), SAED pattern (f), and Li and C K-edge EEL spectra (from the selected rectangular region in [e]) after the first full discharge (D1st) (g). h–n) HAADF-STEM images of an Fe_2O_3 quasi-cube before (h) and after (i) the first full charge (C1st), and the corresponding TEM (j) and HRTEM images (k), HAADF-STEM image and EELS maps (l), SAED pattern (m), and Li and C K-edge EEL spectra (from the selected rectangular region in [l]) after the first full charge (C1st) (n).
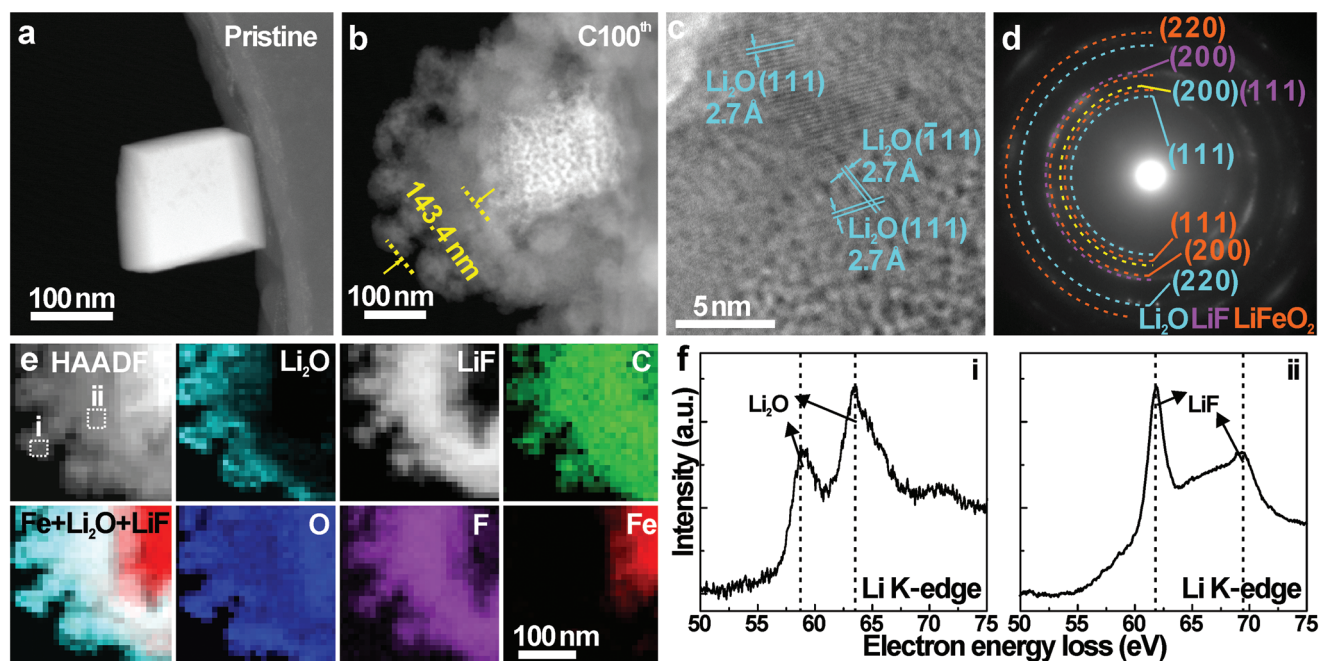
addition to residual Li_2O. Upon further cycling, the SEI layer continues to grow, with the thickness ≈19.6 nm after 40 cycles (Figure S4, Supporting Information) and ≈143.4 nm with the dendrite structure after 100 cycles (**Figure 3**a,b). The $LiFeO_2$ core still maintains integrity after 100 cycles (Figure 3b); thus, the observed capacity loss in Figure 1i is mainly because Li ions become trapped in the growing SEI. On the other hand, the residual Li_2O crystals inside SEI exhibit larger sizes (Figure 3c) after 100 cycles (≈10.2 nm) than those formed after 1 cycle (≈5.1 nm). Moreover, substantial amount of LiF can be detected after 100 cycles by EELS (Figure 3e,f), presumably from accumulated decomposition of $LiPF_6$ electrolyte and lithium alkyl carbonates.[23a] The SEI dendrites grown outside the $LiFeO_2$

core contains C, LiF, and Li_2O, with Li_2O rich on the surface (Figure 3e), which needs to consume a large amount of Li and electrolytes during its formation. The substantial increase of Li_2O and LiF with low ionic conductivity in SEI should be detrimental to ion transport and cause capacity loss.[29] Together with the excessive and continuous growth of SEI, this explains the capacity fading revealed in Figure 1i.

2.2. SEI Breathing on Fe_2O_3@CN

The identified SEI breathing on Fe_2O_3 cycling causes large thickness variation, which is partly due to the incorporation of

**ADVANCED
SCIENCE NEWS**

www.advancedsciencenews.com

**ADVANCED
ENERGY
MATERIALS**

www.advenergymat.de
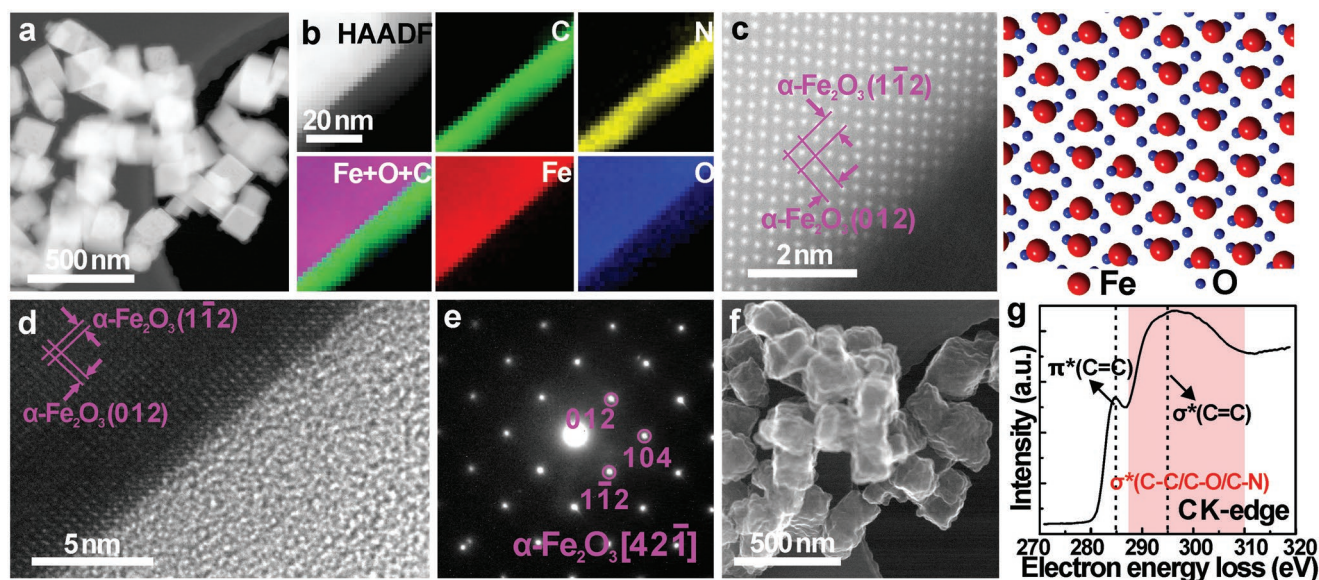
Figure 3. Identical-location cryo-S/TEM characterization of SEI formed on bare Fe_2O_3 quasi-cube after 100 cycles. a–f) HAADF-STEM images on an Fe_2O_3 quasi-cube before (a) and after 100 times full charge (C100th) (b), and the corresponding HRTEM image (c), SAED pattern (d), HAADF-STEM image and EELS maps (e), and Li K-edge EEL spectra (from the two selected rectangular regions in [e]) after 100 times full charge (C100th) (f).

a large amount of Li_2O from lithiation. This may prevent the formation of a steady SEI layer, leading to the continuous SEI growth and the associated capacity loss as observed above. To improve the cycling stability, we apply PPy coating on the surface of Fe_2O_3 quasi-cubes (Figure S5, Supporting Information), aiming to separate the lithiation products from the surface SEI. After carbonization at 400 °C, an amorphous N-doped carbon (CN) layer results with the thickness ≈16 nm (**Figure 4**a,b). The carbon content is determined to be 10.1 wt% by thermogravimetric analysis (TGA, Figure S6, Supporting Information). The basic structure and morphology of α-Fe_2O_3 quasi-cubes remain unaltered during both PPy coating and subsequent carbonization, as revealed by XRD (Figure 1a), aberration-corrected (AC) STEM (Figure 4c), HRTEM (Figure 4d), and SAED (Figure 4e). It should be noted that higher annealing temperature (500 °C and 600 °C) will induce phase transition from α-Fe_2O_3 to γ-Fe_2O_3 (Figures S7–S9, Supporting Information). The CN coating layer leads to the crumpled surface of $Fe_2O_3@$CN revealed by BSE-STEM image (Figure 4f), in contrast to the smooth surface of bare Fe_2O_3 quasi-cubes (Figure 1f). EELS mapping demonstrates uniform distribution of C and N elements in the surface layer of $Fe_2O_3@$CN (Figure 4b), which shows the signs of the C=C bond as well as the potential C−O/C−C/C−N bonds (Figure 4g).[30] $Fe_2O_3@$CN in Li-ion half cells shows similar reversible capacity (936.7 mAh g^{-1}) compared to bare Fe_2O_3, but slightly lower ICE (71.1%) in the first cycle (Figure 1h), which could be attributed to the larger surface area of the crumpled coating layer in contact with electrolytes. The dQ/dV (Figure S10, Supporting Information) and cyclic voltammetry (CV, Figure S11, Supporting Information) curves suggest that this carbon coating layer does not affect the electrochemical mechanism of Fe_2O_3 upon Li storage. On the other hand,

$Fe_2O_3@$CN exhibits excellent cyclic capability, maintaining a high capacity of 1105.4 mAh g^{-1} over 1000 cycles under 1 A g^{-1} (red curve in Figure 1i), in contrast to the obvious capacity degradation in bare Fe_2O_3. The CN coating should have the confinement effect to maintain the integrity of $Fe_2O_3@$CN during cycling. However, as Figure 3b does not show obvious loss of active material, we attribute the distinct cyclic stability of bare Fe_2O_3 and $Fe_2O_3@$CN to their SEI properties tailored by CN coating.

We then explore the discharging/charging behavior of $Fe_2O_3@$CN using identical-location cryo-S/TEM to compare with that of bare Fe_2O_3. As illustrated in **Figure 5**, after the first discharging (lithiation), the $Fe_2O_3@$CN quasi-cube becomes distorted and coarsened, covered by a ≈42.3 nm thick outer layer (Figure 5b), much thicker than the pristine CN coating (≈19.7 nm shown in Figure 5a). HRTEM can resolve a SEI layer only 7.6 nm thick outside CN coating (Figure 5c), which is not only thinner but also denser than that on bare Fe_2O_3 (Figure 2c). It reflects the passivation effect from the CN coating, which could decrease/suppress catalytic effects of electrolyte with Fe nanoparticles formed from the reduction of Fe_2O_3,[31] resulting in a thinner SEI layer.[32] The C K-edge EELS in Figure 5g shows clear difference from that of the pristine $Fe_2O_3@$CN (Figure 4g) but largely resemble those of the discharged Fe_2O_3 (Figure 2g), suggesting similar C species in the formed SEIs (i.e., lithium alkyl carbonates and poly(VC) species). Most excitingly, CN coating does lead to two Li_2O layers as unveiled by EELS (white dashed line in Figure 5e): The outer layer contains discrete Li_2O nanocrystals embedded in the amorphous matrix (Figure 5d), which corresponds to CN coating plus the SEI layer; while, the inner layer consists of dense Li_2O as the lithiation product of Fe_2O_3 (Equation (1)), as evidenced by SAED (Figure 5f). It

**ADVANCED
SCIENCE NEWS**

www.advancedsciencenews.com

**ADVANCED
ENERGY
MATERIALS**

www.advenergymat.de

Figure 4. Characterization of Fe$_2$O$_3$@CN quasi-cubes. a) HAADF-STEM image, b) HAADF-STEM image and EELS maps, c) AC-HAADF-STEM image and the corresponding atomic model of α-Fe$_2$O$_3$, d) HRTEM image, e) SAED pattern, f) BSE-STEM image (the same area as [a]), and g) C K-edge EELS from the surface CN layer on the Fe$_2$O$_3$@CN quasi-cubes.

demonstrates the effectiveness of CN coating in isolating the lithiation products from SEI. The observed thick surface layer in Figure 5b is ascribed to the combination of the Li$_2$O-rich inner layer, the CN coating, and the SEI layer.

SEI breathing is still observed on Fe$_2$O$_3$@CN. After the first charging (de-lithiation), the surface layer thickness decreases to ≈23.4 nm (Figure 5i), only ≈3 nm thicker than the original CN coating (≈20.2 nm, Figure 5h). HRTEM and SAED reveal the presence of LiFeO$_2$ covered by an amorphous C layer without any trace of residual Li$_2$O (Figure 5j,k,m), suggesting the complete conversion of Li$_2$O in contact with the Fe core (Equation (2)). Li K-edge fine structures confirm the absence of Li$_2$O but the presence of Li$_x$C in the SEI (Figure 5n),[33] which is consistent with the nearly identical distribution of Li and C shown in Figure 5l. This indicates that the reduced Li tends to intercalate into CN coating to form amorphous Li$_x$C,[34] which makes it difficult for de-lithiation owing to the slow kinetics of Li deintercalation from the amorphous Li$_x$C.[35] The C K-edge EELS (Figure 5n) exhibit the characteristics of amorphous C without C=O signals, similar to the pristine CN coating shown in Figure 4g. It evinces that the C signal mostly comes from CN coating containing Li$_x$C, with little contribution from residual SEI after the first cycle, in accordance with the small thickness increase detected in Figure 5i. With little SEI formed after the first cycle, the detected SEI components from discharging, such as Li$_2$O and carbon species with C=O bonding, should reversibly participate in the electrochemical reactions during de-lithiation; and thus, cause SEI breathing. The irreversible capacity (Figure 1h) measured from the first cycle may be mainly attributed to the irreversible formation of Li$_x$C in CN coating.

When completing the 10th discharge on Fe$_2$O$_3$@CN (Figure S12a,b, Supporting Information), an ≈16.7 nm SEI layer outside CN coating can be seen (Figure S12c, Supporting Information), with Li$_2$O nanocrystals embedded (Figure S12d, Supporting Information). CN coating still confines plenty of

Li$_2$O as an inner layer (Figure S12e, Supporting Information). After the 10th charging, a thin SEI layer (≈4.0 nm) containing Li$_2$O remains outside CN coating (Figure S12g–j, Supporting Information), in contrast to the indistinguishable SEI after the first cycle (Figure 5j). It suggests that SEI on Fe$_2$O$_3$@CN develops in a slower way than on bare Fe$_2$O$_3$, probably because CN coating is chemically more stable than the α-Fe$_2$O$_3$ surface that has substantial catalytic activity.[36] The Li$_x$C phase is also detected due to Li intercalation into CN coating (Figure S12k, Supporting Information). Upon further cycling on Fe$_2$O$_3$@CN, the SEI layer after 40 cycles largely resembled that formed after 10 cycles, with the thin Li$_2$O-contained SEI layer forming outside the Li$_x$C-contained CN coating (Figure S13, Supporting Information). The scanning electron microscopy (SEM, Figure S14, Supporting Information) further evidences that the overall morphologies of Fe$_2$O$_3$@CN electrode are almost unchanged after 40 cycles. This structure remains stable after 100 (**Figure 6**) and 200 cycles (Figure S15, Supporting Information), which should facilitate the fast ion transfer and improve the long-term electrochemical stability. Therefore, the remarkably improved cyclic stability of Fe$_2$O$_3$@CN is attributed not only to the formation of the thin SEI layer from the passivation effect of CN coating but also to the more steady SEI behavior, presumably due to the effective separation of lithiation products from the SEI layer. No LiF is detected for Fe$_2$O$_3$@CN even after long-term cycling, indicating suppressed decomposition of the electrolyte (Figure S16b, Supporting Information).

2.3. A Comparison of SEI Breathing Behavior

The behavior of SEI breathing on both Fe$_2$O$_3$ and Fe$_2$O$_3$@CN is summarized in **Figure 7**. With the size of Fe$_2$O$_3$ cores and thickness of SEIs derived as illustrated in Figure 7a,b, both quantities
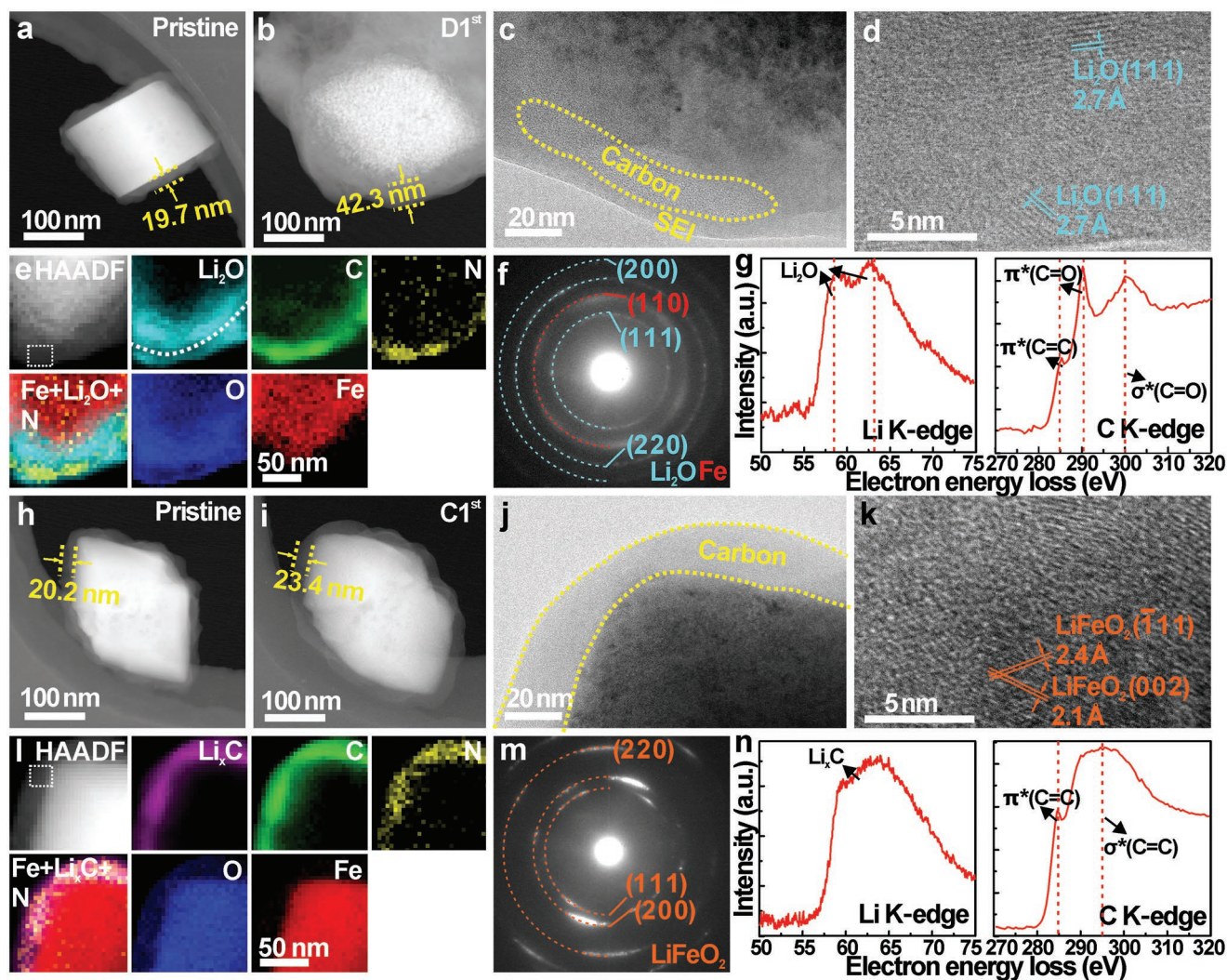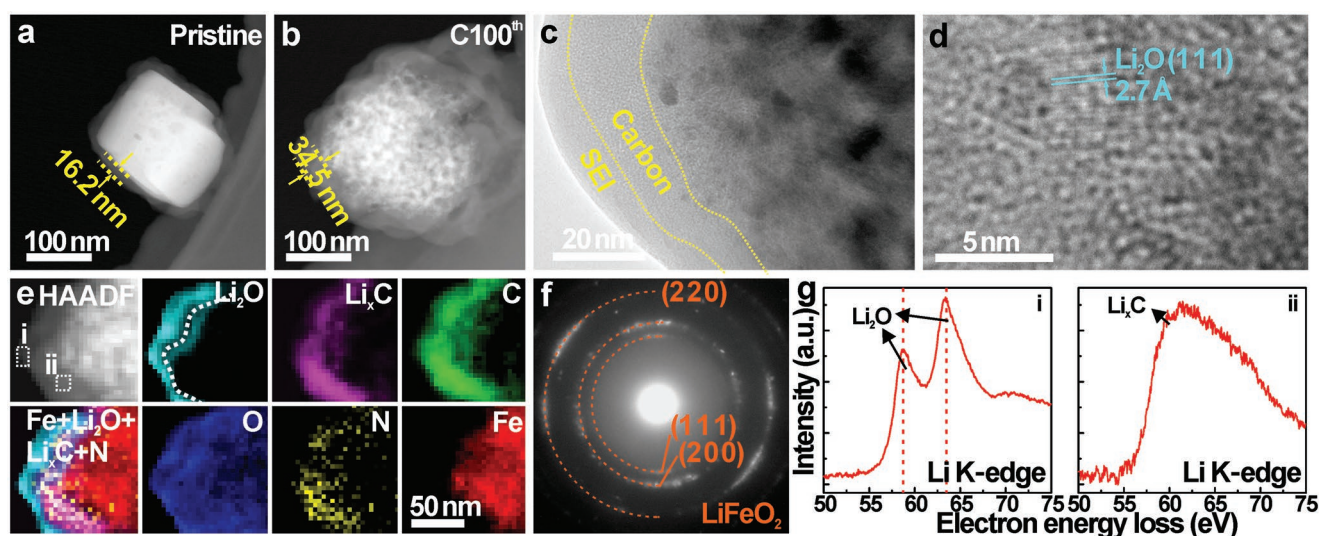
Figure 5. Identical-location cryo-S/TEM characterization of SEI formed on Fe_2O_3@CN quasi-cubes in the first cycle. a–g) HAADF-STEM images of an Fe_2O_3@CN quasi-cube before (a) and after the first full discharge (D1st) (b), and the corresponding TEM (c) and HRTEM images (d). HAADF-STEM image and EELS maps (e), SAED pattern (f), and Li and C K-edge EEL spectra (from the selected rectangular region in [e]) after the first full discharge (D1st) (g). h–n) HAADF-STEM images of an Fe_2O_3@CN quasi-cube before (h) and after the first full charge (C1st) (i), and the corresponding TEM (j) and HRTEM images (k), HAADF-STEM image and EELS maps (l), SAED pattern (m), and Li and C K-edge EEL spectra (from the selected rectangular region in [l]) after the first full charge (C1st) (n).

increase after discharging and decrease after charging, manifesting the oscillation or breathing behavior as shown in the yellow regions in Figure 7c,d. As illustrated in previous sections, such SEI breathing is mainly associated with the reversible reaction of C=O containing species and Li_2O in SEIs, which accounts for the higher than the theoretical value for Fe_2O_3 (848 mAh g^{-1} for forming $LiFeO_2$). Bare Fe_2O_3 exhibits larger volume expansion as well as SEI thickness variation, the latter of which is largely due to the incorporation of lithiation product Li_2O in SEI. Such unstable SEI evolves into the dendrite morphology with large thickness after 100 cycles, causing capacity fading in bare Fe_2O_3. Using CN coating to effectively separate the lithiation product from SEI, a much more steady SEI breathing behavior is achieved in Fe_2O_3@CN (Figure 7d), explaining its excellent cycling stability. The passivation effect of CN coating may also facilitate the formation of the thinner
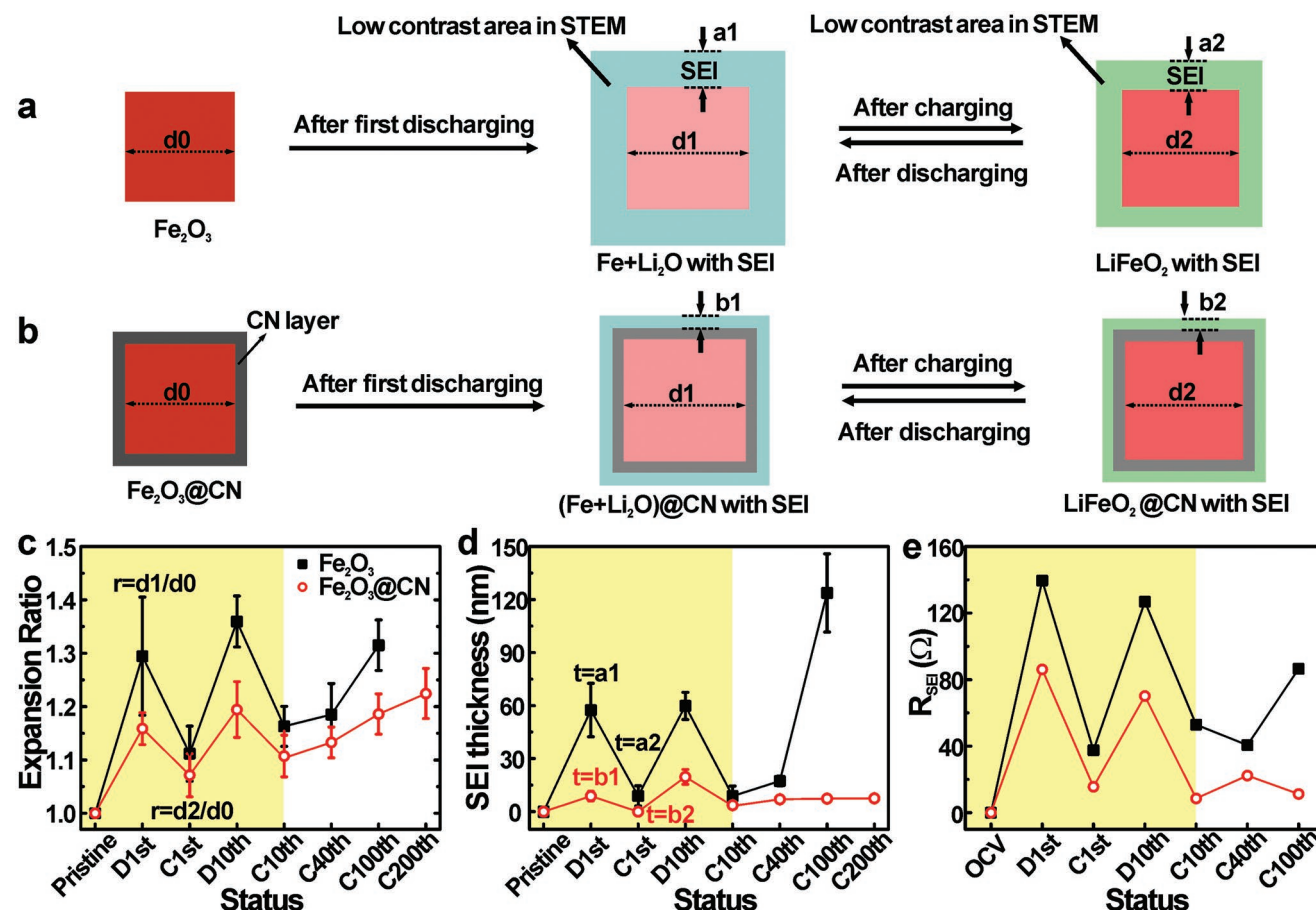
SEI layer (a1,2 > b1,2), in addition to the separation of the lithiation product from SEI.

Besides the smaller variation in SEI thickness, Fe_2O_3@CN also shows stable SEI composition upon cycling as revealed by EELS fine structures summarized in **Figure 8** Figure S16, Supporting Information. For bare Fe_2O_3 after cycling, the Li K-edge shows that the dominant Li species in SEI are Li_2O, until 100 cycles when substantial LiF signal is detected from the decomposition of $LiPF_6$ electrolyte and lithium alkyl carbonates (Figure 8a).[37] The F K-edge signal further confirms the presence of F species (Figure S16a, Supporting Information). The lithium alkyl carbonates decomposition is also verified by the C K-edge fine structures, exhibiting the relatively decreasing C=O signal compared to the C=C signal with more cycling (Figure 8b). This reflects that the C=O containing species such as poly(VC)) and lithium alkyl carbonates are decreasing

Figure 6. Identical-location cryo-S/TEM characterization of SEI formed on an Fe_2O_3@CN quasi-cube after 100 cycles. a–g) HAADF-STEM images of an Fe_2O_3 quasi-cube before (a) and after (b) 100 times full charge (C100th), and the corresponding TEM (c) and HRTEM images (d), HAADF-STEM image and EELS maps (e), SAED pattern (f), and Li K-edge EEL spectra (from the selected rectangular region in [e]) after 100 times full charge (C100th) (g).

Figure 7. a,b) Schemes of SEI formation on bare Fe_2O_3 (a) and Fe_2O_3@CN quasi-cubes (b), with the cube size and SEI layer thickness indicated by various parameters. c–e) Plots of expansion ratio calculated by d1/d0 for discharged states and d2/d0 for charged states (c), SEI thickness calculated by a1 and a2 for bare Fe_2O_3 and b1 and b2 for Fe_2O_3@CN (d), and SEI resistance of Fe_2O_3 and Fe_2O_3@CN at different cycling stages (e).

Figure 8. Comparison of EEL spectra of a,c) Li K-edge and b,d) C K-edge from bare Fe_2O_3 (a,b) and Fe_2O_3@CN (c,d) surfaces after charging.

in the cyclic reactions. Together with more LiF formation, it evinces a gradual transition from organic into inorganic-type SEI for Fe_2O_3 during long-term cycling. This contradicts the earlier XPS study on Fe_2O_3 which suggests a stable SEI composition upon cycling.[15a] In contrast, Fe_2O_3@CN develops stable SEI consisting of Li_2O (Figure 8c), C species consistently (Figure 8d), and negligible F species (Figure S16b, Supporting Information), with no substantial change up to 200 cycles. Especially, the decomposition products with both C=C and C=O binding are well kept during the cycling, evincing a stable SEI formation on the Fe_2O_3@CN surface. Such a SEI with abundant organic and inorganic species can not only enhance the elastomeric properties but also facilitate fast Li diffusion. Therefore, the lack of organic-to-inorganic SEI transition in Fe_2O_3@CN should result in both higher cycling stability (Figure 1i) and lower SEI resistivity.

To further interrogate the effect of SEI breathing on SEI resistivity, we have performed electrochemical impedance spectroscopy (EIS) measurements after different cycles. As presented in Figures S17–S20, Supporting Information, the semicircle existing at high frequencies typically reflects the resistance of SEI (R2 in Figure S20, Supporting Information) and the following semicircle at middle frequencies is related to the resistance of interfacial charge transfer.[38] Two semicircles are present for both samples after the first and 10th discharging

(Figure S18a,c, Supporting Information), indicating considerable resistances for both SEIs and interfacial charge transfer. On the contrary, for samples at the fully charged states (C1st, C10st, and C40th in Figure S18b,d,e, Supporting Information), there is only one semicircle at high frequencies representing the resistance of SEIs, while the charge transfer resistance becomes unobservable suggesting that the electrodes are fully de-lithiated.[39] For bare Fe_2O_3 after the 100th charging (Figures S18f and Figure S19, Supporting Information), the increased SEI resistance is observed from the thick SEI layer with abundant Li_2O and LiF (Figure 3). Moreover, the large charge transfer resistance is observed for this sample, possibly due to the irretrievable de-lithiation reactions. Overall, the derived SEI resistance (Figure 7e) closely follows the variation of SEI thickness (Figure 7d) for both samples, with Fe_2O_3@CN always showing lower resistance, demonstrating the effect of SEI breathing on the transport properties.

3. Conclusion

In conclusion, applying identical-location cryo-S/TEM on bare Fe_2O_3 and Fe_2O_3@CN quasi-cubes, we have quantitatively measured the SEI thickness variations induced by discharging (lithiation)/charging (de-lithiation) cycling, representing the

typical breathing behavior of SEIs whose origin is identified as the reversible reactions of C=O containing species and Li_2O in SEIs. An unstable SEI layer develops on bare Fe_2O_3 with a larger thickness variation upon breathing, which can be attributed to the intermixing with the lithiation product Li_2O. It further leads to continuous and excessive SEI growth upon cycling, resulting in the substantial capacity loss within 100 cycles. A transition from organic to inorganic-type SEI is also identified upon cycling on bare Fe_2O_3, which gives rise to the larger SEI resistance. With CN coating to passivate the Fe_2O_3 surface, the lithiation product Li_2O can be effectively separated from SEI, resulting in a thinner SEI layer with more steady breathing behavior and less compositional variation upon cycling. Superior cycling stability is achieved on $Fe_2O_3@CN$ compared to bare Fe_2O_3. Our work highlights the significance of understanding and tailoring the dynamic behavior of SEIs such as SEI breathing to achieve optimal battery performance.

4. Experimental Section

Fe_2O_3 Quasi-Cubes Synthesis: Fe_2O_3 quasi-cubes were fabricated by a modified one-step hydrothermal method.[40] Concretely, 0.808 g of $Fe(NO_3)_3 \cdot 9H_2O$ (98.0-101.0%, Alfa Aesar) and 0.125 g of $Ni(OAc)_2 \cdot 4H_2O$ (98+%, Alfa Aesar) were first dissolved in 10 mL of deionized (DI) water to prepare a transparent solution. Afterward, 9 mL of ammonia solution (28%, Alfa Aesar) was added drop by drop to the above solution under magnetic stirring for 10 min. Then, the mixed solution was transferred into a 50 mL Teflon lined stainless steel autoclave and kept at 160 °C for 12 h. After cooling to room temperature, the precipitates were collected by centrifugation and washed with DI water and alcohol three times. Last, the red precipitates were dried under vacuum at 60 °C.

$Fe_2O_3@PPy$ Quasi-Cubes Synthesis: The coating of polypyrrole (PPy) on the as-fabricated Fe_2O_3 quasi-cubes was achieved based on a modified method from previous work.[41] To prepare 5% polyvinyl alcohol (PVA, M_W 89 000–98 000, 99+%, Sigma–Aldrich) aqueous solution, 5 g of PVA and 95 mL of DI water were added to a round-bottomed flask under magnetic stirring and were heated to 95 °C with condensing reflux until the solution turned fully transparent (≈4 h). 50 mg of as-fabricated Fe_2O_3 quasi-cubes was added to a beaker that contained 90 mL of DI water, 10 mg of sodium dodecyl sulfate (SDS, ≥99.0%, Sigma–Aldrich), and 10 mL of cooled 5% PVA solution. This mixer was first dispersed under ultrasonication for 30 min and magnetic stirring for 2 h. Then, it was transferred to a 0 °C ice bath under stirring for at least 1 h for cooling down before adding 150 µL of pyrrole (98%, Sigma–Aldrich) precursor. After stirring for 20 min to get a homogeneous dispersion, 10 mL of 0.03 mm $FeCl_3$ ($FeCl_3 \cdot 6H_2O$, 97%, Alfa Aesar) aqueous solution was added dropwise to initiate the polymerization. The solution was under ultrasonication for 10 min and stirred for another 2 h for a complete reaction in the ice bath. The synthesized $Fe_2O_3@PPy$ samples were centrifugated, washed with hot DI water three times, and dried under vacuum at 60 °C.

$Fe_2O_3@CN$ Quasi-Cubes Synthesis: The $Fe_2O_3@CN$ quasi-cubes were fabricated by annealing the prepared $Fe_2O_3@PPy$ in a tube furnace at 400 °C / 500 °C / 600 °C for 3 h under the N_2 atmosphere with a heating rate of 10 °C min^{-1}.

Electrochemical Measurements: The coin cells were assembled using CR2032 battery cases with an active material electrode as the working electrode and a metallic Li plate as the counter/reference electrode. The active material, super P, vapor grown carbon fibers (VGCF), and sodium carboxymethyl cellulose (CMC) were mixed by hand grinding with the mass ratio of 7: 1: 1: 1 in a mortar and the slurry was cast on Cu foil to make the electrodes. The electrodes with a 12 mm diameter and ≈1 mg cm^{-2} mass loading were used for coin cell assembling. Lithium

hexafluorophosphate ($LiPF_6$), EC, dimethyl carbonate (DMC), and ethyl methyl carbonate (EMC) were purchased from DoDo Chem and FEC was bought from Alfa Aesar. 1 m $LiPF_6$ in EC: DMC: EMC (volume ratio of 1: 1: 1) with 5 vol% FEC was applied as the electrolyte. One piece of GF/D (Whatman) coupled with one piece of Celgard 2325 was used as the separator. The galvanostatic charge/discharge was measured on LAND battery testing system within 0–3V. EIS was performed on a Biologic SP150 electrochemical workstation (100kHz-0.1Hz) with an amplitude of 5 mV. CV was performed on Biologic VMP-300 within 0–3 V at scan rate of 0.1 mV s^{-1}.

Material Characterization: XRD patterns were collected on Rigaku SmartLab X-ray Diffractometer with a Cu target. The TGA was carried out on PerkinElmer Pyris 1 TGA in air atmosphere from 30 °C to 800 °C with heating rate of 10 °C min^{-1}. The SEM was observed by Zeiss Ultra plus with acceleration voltage of 5 kV and InLens detector.

Identical-Location Cryo-S/TEM Characterization: S/TEM characterization was performed on a 200kV JEOL JEM-2100F microscope, equipped with a Gatan Enfina electron spectrometer. EELS mapping was carried out in STEM mode with a 13 mrad convergence angle for the optimal probe condition. A 21 mrad collection angle was used for EELS acquisition and an 89 mrad inner angle was used for HAADF images collection, which could be acquired simultaneously for STEM-EELS elemental mapping. Besides normal elemental mapping, the EELS fine-structure maps for Li_2O, LiF, and Li_xC were obtained using multiple linear least-square fitting in DigitalMicrograph (Gatan) software with the corresponding reference spectra. AC-HAADF-STEM characterization was performed on a ThermoFisher Scientific Spectra 300 microscope equipped with an X-FEG/UltiMono electron source and a CEOS SCORR fifth-order probe corrector, operated at 300 kV. A 24 mrad convergence angle and the 45–200 mrad collection angle were used for atomic-resolution HAADF-STEM imaging.

The Fe_2O_3 and $Fe_2O_3@CN$ TEM samples were first dispersed on holey carbon film-coated Cu grids. At least eight particles on one grid were selected and examined by S/TEM before assembling into the battery for discharging/charging cycling. After discharging/charging, the grid was promptly taken out from the disassembled cell to avoid the possible dissolution reaction and was mildly washed with the DMC solvent in an Ar-filled glovebox to remove the excess electrolyte. Afterward, the grid was transferred to a liquid nitrogen cooling holder (Gatan, model 636) and sealed with a plastic cap wrapped by the Parafilm tape. Once out of the glovebox, the holder was inserted into TEM as quickly as possible to minimize air exposure. The system was stabilized for at least 40 min after adding liquid nitrogen and the observation was carried out under ≈ −175 °C.

Supporting Information

Supporting Information is available from the Wiley Online Library or from the author.

Acknowledgements

Conflict of Interest

The authors declare no conflict of interest.

Data Availability Statement

The data that support the findings of this study are available from the corresponding author upon reasonable request.

Keywords

[1] a) E. Peled, S. Menkin, *J. Electrochem. Soc.* **2017**, *164*, A1703; b) Y. S. Meng, V. Srinivasan, K. Xu, *Science* **2022**, *378*, eabq3750.

[2] J. B. Goodenough, Y. Kim, *Chem. Mater.* **2010**, *22*, 587.

[3] K. Xu, *Chem. Rev.* **2014**, *114*, 11503.

[4] X. Li, X. Sun, X. Hu, F. Fan, S. Cai, C. Zheng, G. D. Stucky, *Nano Energy* **2020**, *77*, 105143.

[5] M. Winter, *Z. Phys. Chem.* **2009**, *223*, 1395.

[6] a) S. Tan, J. M. Kim, A. Corrao, S. Ghose, H. Zhong, N. Rui, X. Wang, S. Senanayake, B. J. Polzin, P. Khalifah, J. Xiao, J. Liu, K. Xu, X. Q. Yang, X. Cao, E. Hu, *Nat. Nanotechnol.* **2022**, *18*, 243; b) Z. Shadike, H. Lee, O. Borodin, X. Cao, X. Fan, X. Wang, R. Lin, S.-M. Bak, S. Ghose, K. Xu, *Nat. Nanotechnol.* **2021**, *16*, 549; c) C. Gong, S. D. Pu, X. Gao, S. Yang, J. Liu, Z. Ning, G. J. Rees, I. Capone, L. Pi, B. Liu, *Adv. Energy Mater.* **2021**, *11*, 2003118; d) J. Wan, Z. Zuo, Z.-Z. Shen, W.-P. Chen, G.-X. Liu, X.-C. Hu, Y.-X. Song, S. Xin, Y.-G. Guo, R. Wen, *J. Am. Chem. Soc.* **2022**, *144*, 9354; e) T. Liu, L. Lin, X. Bi, L. Tian, K. Yang, J. Liu, M. Li, Z. Chen, J. Lu, K. Amine, *Nat. Nanotechnol.* **2019**, *14*, 50; f) X. Du, Y. Gao, Z. Hou, X. Guo, Y. Zhu, B. Zhang, *ACS Appl. Energy Mater.* **2022**, *5*, 2252; g) X. Du, B. Zhang, *ACS Nano* **2021**, *15*, 16851.

[7] Z. Yu, P. E. Rudnicki, Z. Zhang, Z. Huang, H. Celik, S. T. Oyakhire, Y. Chen, X. Kong, S. C. Kim, X. Xiao, *Nat. Energy* **2022**, *7*, 94.

[8] Y. Li, Y. Li, A. Pei, K. Yan, Y. Sun, C.-L. Wu, L.-M. Joubert, R. Chin, A. L. Koh, Y. Yu, *Science* **2017**, *358*, 506.

[9] L. Wang, A. Menakath, F. Han, Y. Wang, P. Y. Zavalij, K. J. Gaskell, O. Borodin, D. Iuga, S. P. Brown, C. Wang, *Nat. Chem.* **2019**, *11*, 789.

[10] a) C. S. Santos, A. Botz, A. S. Bandarenka, E. Ventosa, W. Schuhmann, *Angew. Chem., Int. Ed.* **2022**, *61*, e202202744; b) J. Huang, X. Guo, X. Du, X. Lin, J.-Q. Huang, H. Tan, Y. Zhu, B. Zhang, *Energy Environ. Sci.* **2019**, *12*, 1550; c) Y. Gao, X. Du, Z. Hou, X. Shen, Y.-W. Mai, J.-M. Tarascon, B. Zhang, *Joule* **2021**, *5*, 1860.

[11] J. D. McBrayer, M.-T. F. Rodrigues, M. C. Schulze, D. P. Abraham, C. A. Apblett, I. Bloom, G. M. Carroll, A. M. Colclasure, C. Fang, K. L. Harrison, *Nat. Energy* **2021**, *6*, 866.

[12] a) D. Alliata, R. Kötz, P. Novák, H. Siegenthaler, *Electrochem. Commun.* **2000**, *2*, 436; b) J. Lei, L. Li, R. Kostecki, R. Muller, F. McLarnon, *J. Electrochem. Soc.* **2005**, *152*, A774; c) B. M. Meyer, N. Leifer, S. Sakamoto, S. G. Greenbaum, C. P. Grey, *Electrochem. Solid-State Lett.* **2005**, *8*, A145; d) L. Zhao, I. Watanabe, T. Doi, S. Okada, J.-I. Yamaki, *J. Power Sources* **2006**, *161*, 1275.

[13] H. Bryngelsson, M. Stjerndahl, T. Gustafsson, K. Edström, *J. Power Sources* **2007**, *174*, 970.

[14] Y. Ein-Eli, *Electrochem. Solid-State Lett.* **1999**, *2*, 212.

[15] a) B. Tian, J. Światowska, V. Maurice, S. Zanna, A. Seyeux, L. H. Klein, P. Marcus, *J. Phys. Chem. C* **2013**, *117*, 21651; b) T. Fears, M. Doucet, J. Browning, J. Baldwin, J. G. Winiarz, H. Kaiser, H. Taub, R. Sacci, G. Veith, *Phys. Chem. Chem. Phys.* **2016**, *18*, 13927;

[16] c) G. M. Veith, M. Doucet, J. K. Baldwin, R. L. Sacci, T. M. Fears, Y. Wang, J. F. Browning, *J. Phys. Chem. C* **2015**, *119*, 20339; d) C. Cao, H. G. Steinrück, B. Shyam, M. F. Toney, *Adv. Mater. Interfaces* **2017**, *4*, 1700771.

[16] a) W. Huang, J. Wang, M. R. Braun, Z. Zhang, Y. Li, D. T. Boyle, P. C. McIntyre, Y. Cui, *Matter* **2019**, *1*, 1232; b) S. Ji, J. Li, J. Li, C. Song, S. Wang, K. Wang, K. S. Hui, C. Zha, Y. Zheng, D. A. Dinh, *Adv. Funct. Mater.* **2022**, *32*, 2200771; c) K. Yang, X. Zhang, K. Song, J. Zhang, C. Liu, L. Mi, Y. Wang, W. Chen, *Electrochim. Acta* **2020**, *337*, 135783; d) Q. Guo, Y. Ma, T. Chen, Q. Xia, M. Yang, H. Xia, Y. Yu, *ACS Nano* **2017**, *11*, 12658.

[17] H. Kim, W. Choi, J. Yoon, J. H. Um, W. Lee, J. Kim, J. Cabana, W.-S. Yoon, *Chem. Rev.* **2020**, *120*, 6934.

[18] a) R. Lin, Y. He, C. Wang, P. Zou, E. Hu, X.-Q. Yang, K. Xu, H. L. Xin, *Nat. Nanotechnol.* **2022**, *17*, 768; b) X. C. Ren, X. Q. Zhang, R. Xu, J. Q. Huang, Q. Zhang, *Adv. Mater.* **2020**, *32*, 1908293; c) Z. Zhang, Y. Cui, R. Vila, Y. Li, W. Zhang, W. Zhou, W. Chiu, Y. Cui, *Acc. Chem. Res.* **2021**, *54*, 3505; d) D. Cheng, B. Lu, G. Raghavendran, M. Zhang, Y. S. Meng, *Matter* **2022**, *5*, 26; e) B. Han, Y. Zou, G. Xu, S. Hu, Y. Kang, Y. Qian, J. Wu, X. Ma, J. Yao, T. Li, *Energy Environ. Sci.* **2021**, *14*, 4882; f) Z. Ju, H. Yuan, O. Sheng, T. Liu, J. Nai, Y. Wang, Y. Liu, X. Tao, *Small Sci.* **2021**, *1*, 2100055.

[19] Y. He, L. Jiang, T. Chen, Y. Xu, H. Jia, R. Yi, D. Xue, M. Song, A. Genc, C. Bouchet-Marquis, *Nat. Nanotechnol.* **2021**, *16*, 1113.

[20] a) B. Han, X. Li, S. Bai, Y. Zou, B. Lu, M. Zhang, X. Ma, Z. Chang, Y. S. Meng, M. Gu, *Matter* **2021**, *4*, 3741; b) Z. Zhang, Y. Li, R. Xu, W. Zhou, Y. Li, S. T. Oyakhire, Y. Wu, J. Xu, H. Wang, Z. Yu, *Science* **2022**, *375*, 66; c) Z. Ju, C. Jin, H. Yuan, T. Yang, O. Sheng, T. Liu, Y. Liu, Y. Wang, F. Ma, W. Zhang, *Chem. Eng. J.* **2021**, *408*, 128016; d) Z. Ju, C. Jin, X. Cai, O. Sheng, J. Wang, J. Luo, H. Yuan, G. Lu, X. Tao, Z. Liang, *ACS Energy Lett.* **2022**, *8*, 486.

[21] a) H. Xu, S. Li, C. Zhang, X. Chen, W. Liu, Y. Zheng, Y. Xie, Y. Huang, J. Li, *Energy Environ. Sci.* **2019**, *12*, 2991; b) E. J. McShane, H. K. Bergstrom, P. J. Weddle, D. E. Brown, A. M. Colclasure, B. D. McCloskey, *ACS Energy Lett.* **2022**, *7*, 2734.

[22] Y. Xu, H. Wu, Y. He, Q. Chen, J.-G. Zhang, W. Xu, C. Wang, *Nano Lett.* **2019**, *20*, 418.

[23] a) S. K. Heiskanen, J. Kim, B. L. Lucht, *Joule* **2019**, *3*, 2322; b) J. Henschel, C. Peschel, S. Klein, F. Horsthemke, M. Winter, S. Nowak, *Angew. Chem., Int. Ed.* **2020**, *59*, 6128.

[24] Y. Jin, N.-J. H. Kneusels, P. C. Magusin, G. Kim, E. Castillo-Martínez, L. E. Marbella, R. N. Kerber, D. J. Howe, S. Paul, T. Liu, *J. Am. Chem. Soc.* **2017**, *139*, 14992.

[25] a) D. Aurbach, *J. Power Sources* **2000**, *89*, 206; b) V. Etacheri, O. Haik, Y. Goffer, G. A. Roberts, I. C. Stefan, R. Fasching, D. Aurbach, *Langmuir* **2012**, *28*, 965.

[26] Z. Liu, Q. Cheng, K. Li, Y. Wang, J. Zhang, *Powder Technol.* **2020**, *367*, 97.

[27] A. Brandt, F. Winter, S. Klamor, F. Berkemeier, J. Rana, R. Pöttgen, A. Balducci, *J. Mater. Chem. A* **2013**, *1*, 11229.

[28] M. S. Whittingham, *Chem. Rev.* **2004**, *104*, 4271.

[29] M. He, R. Guo, G. M. Hobold, H. Gao, B. M. Gallant, *Proc. Natl. Acad. Sci. U. S. A.* **2020**, *117*, 73.

[30] J. Gao, Y. Wang, H. Wu, X. Liu, L. Wang, Q. Yu, A. Li, H. Wang, C. Song, Z. Gao, *Angew. Chem.* **2019**, *131*, 15233.

[31] A. Ponrouch, A. R. Goñi, M. T. Sougrati, M. Ati, J.-M. Tarascon, J. Nava-Avendano, M. R. Palacín, *Energy Environ. Sci.* **2013**, *6*, 3363.

[32] Y.-B. He, F. Ning, B. Li, Q.-S. Song, W. Lv, H. Du, D. Zhai, F. Su, Q.-H. Yang, F. Kang, *J. Power Sources* **2012**, *202*, 253.

[33] J. Kwon, W. J. Lee, S. O. Kim, *J. Phys. Chem. C* **2019**, *123*, 6220.

[34] B. Philippe, M. Valvo, F. Lindgren, H. K. Rensmo, K. Edström, *Chem. Mater.* **2014**, *26*, 5028.

[35] S. Alvin, H. S. Cahyadi, J. Hwang, W. Chang, S. K. Kwak, J. Kim, *Adv. Energy Mater.* **2020**, *10*, 2000283.

[36] H. Li, H. Zhou, *Chem* **2012**, *48*, 1201.

[37] R. A. Vilá, W. Huang, Y. Cui, *Cell Rep. Phys. Sci.* **2020**, *1*, 100188.

[38] Y. Wang, Z. Wang, Y. Chen, H. Zhang, M. Yousaf, H. Wu, M. Zou, A. Cao, R. P. Han, *Adv. Mater.* **2018**, *30*, 1802074.

[39] S. S. Zhang, K. Xu, T. Jow, *Electrochim. Acta* **2006**, *51*, 1636.

[40] R. Liu, Y. Jiang, Q. Chen, Q. Lu, W. Du, F. Gao, *RSC Adv.* **2013**, *3*, 8261.

[41] Y. Wang, Y. Xiao, R. Tang, *Eur. J. Chem.* **2014**, *20*, 11826.